Monthly Notices of the ROYAL ASTRONOMICAL SOCIETY

Mon. Not. R. Astron. Soc. **426,** 892–902 (2012) doi:10.1111/j.1365-2966.2012.21696.x

The heating of dust by old stellar populations in the bulge of M31

Brent Groves,[1]★ Oliver Krause,[1] Karin Sandstrom,[1] Anika Schmiedeke,[1,2] Adam Leroy,[3] Hendrik Linz,[1] Maria Kapala,[1] Hans-Walter Rix,[1] Eva Schinnerer,[1] Fatemeh Tabatabaei,[1] Fabian Walter[1] and Elisabete da Cunha[1]

[1]*Max Planck Institute for Astronomy, Königstuhl 17, D-69117 Heidelberg, Germany*
[2]*Universität zu Köln, Zülpicher Strasse 77, 50937 Köln, Germany*
[3]*National Radio Astronomy Observatory, Charlottesville, VA 22903, USA*

Accepted 2012 July 10. Received 2012 June 15; in original form 2012 March 14

ABSTRACT

We use new *Herschel* multiband imaging of the Andromeda galaxy to analyse how dust heating occurs in the central regions of galaxy spheroids that are essentially devoid of young stars. We construct a dust temperature map of M31 through fitting modified blackbodies to the *Herschel* data, and find that the temperature within 2 kpc rises strongly from the mean value in the disc of 17 ± 1 to $\sim$35 K at the centre. Ultraviolet (UV) to near-infrared (IR) imaging of the central few kpc shows directly the absence of young stellar populations, delineates the radial profile of the stellar density and demonstrates that even the near-UV dust extinction is optically thin in M31's bulge. This allows the direct calculation of the stellar radiation heating in the bulge, $U_*(r)$, as a function of radius. The increasing temperature profile in the centre matches that expected from the stellar heating, i.e. that the dust heating and cooling rates track each other over nearly two orders of magnitude in U_*. The modelled dust heating is in excess of the observed dust temperatures, suggesting that it is more than sufficient to explain the observed IR emission. Together with the wavelength-dependent absorption cross-section of the dust, this demonstrates directly that it is the optical, not UV, radiation that sets the heating rate. This analysis shows that neither young stellar populations nor stellar near-UV radiation is necessary to heat dust to warm temperatures in galaxy spheroids. Rather, it is the high densities of Gyr-old stellar populations that provide a sufficiently strong diffuse radiation field to heat the dust. To the extent which these results pertain to the tenuous dust found in the centres of early-type galaxies remains yet to be explored.

Key words: galaxies: bulges – galaxies: individual: M31 – galaxies: ISM – infrared: galaxies.

1 INTRODUCTION

As the nearest, massive galaxy, Andromeda (M31, NGC 224) has offered a unique insight into the properties of galaxies. It provides the perfect stepping stone between the well-resolved interstellar medium (ISM) and stellar populations within our own Galaxy, and the integrated properties of more distant galaxies. Because of its proximity ($\sim$780 kpc), Andromeda offers more than a resolved example of an early-type spiral galaxy, but can also be used to explore the interaction of the ISM and stars in early-type galaxies (ETGs) through its large, visually dominant bulge.

Andromeda's bulge dominates the stellar luminosity and mass within the central 1.5 kpc ($R_{\rm eff}$(bulge) $\sim$ 0.5–1.1 kpc; Courteau et al. 2011), with the disc dominating beyond this. The bulge contributes $\sim$30 per cent of the total stellar mass and luminosity in M31, and it is clearly the highest surface brightness feature at ultraviolet (UV)–near-infrared (NIR) wavelengths (Geehan et al. 2006; Courteau et al. 2011). While the integrated colours and luminosity of M31 may place the galaxy in the 'green valley' (Mutch, Croton & Poole 2011), the optical colours of the bulge are red, with a $B - V \approx$ 0.9–1.0 (Walterbos & Kennicutt 1987), placing it securely in the range of the red sequence, where most ETGs are found. Oke & Sandage (1968) even used the spectral energy distribution (SED) of the centre of M31 as a representative for the average giant elliptical galaxy when determining K-corrections.

This 'early-type' nature of the bulge is supported by the old mean stellar age determined for the central region of M31. Resolved star colour–magnitude diagrams created by ground-based, adaptive-optics, NIR imaging reveal a population dominated by stars greater than 6 Gyr (Davidge et al. 2005; Olsen et al. 2006), while single-stellar population fits to absorption-line indices from

★E-mail: brent@mpia.de

slit spectroscopy of the bulge (Saglia et al. 2010) find that the bulge of M31 is uniformly old ($\geq$12 Gyr, excluding the central arcsec). High resolution, individual star photometry from the Panchromatic Hubble Andromeda Treasury (PHAT) survey (Dalcanton et al. 2012) find no population of young stellar sources, with the UV light dominated by evolved stars such as post-asymptotic giant branch (AGB) stars (Rosenfield et al. 2012).

Given this lack of young stars and star formation, it is unsurprising that the bulge of M31 is also extremely gas poor. Little to no CO is detected in the CO(1–0) map of Nieten et al. (2006) down to low surface brightnesses. CO is detected in the central part of M31 when deeper observations of small high-attenuation regions are made (Melchior et al. 2000; Melchior & Combes 2011); however, the attenuation in these regions is still relatively low ($A_B < 0.3$) and the covering fraction of these regions is very small (Melchior et al. 2000), meaning diffuse, low-attenuation dust (and presumably diffuse gas) is more characteristic of the bulge. Compounding this is a low CO–H_2 ratio (Leroy et al. 2011), and a low total H I column (Braun et al. 2009) giving a total cool gas mass in the centre of only a few $10^6\,M_\odot$ ($\sim$0.02 per cent of the bulge stellar mass), likely dominated by molecular gas (e.g. Li, Wang & Wakker 2009; Melchior & Combes 2011).

This low gas fraction makes the M31 bulge more gas poor than many ETGs, as recent work with the ATLAS3D sample (Cappellari et al. 2011) has demonstrated. Young et al. (2011) observed CO(1–0) in $\sim$22 per cent of the sample of nearby ETGs, giving corresponding gas masses of $M(H_2) > 10^7\,M_\odot$ (for a sample with a median stellar mass of $M_\star = 3 \times 10^{10}\,M_\odot$). Similarly, studies of nearby field ellipticals and lenticulars have found atomic gas in a large fraction of these ($\sim$70 per cent), with this H I emission generally associated with ionized gas emission (Morganti et al. 2006). Interestingly, the molecular gas in ETGs is not always associated with star formation. Optical colours and emission-line ratios indicate other forms of heating in the ISM of some early types, and only low levels, if any, of star formation (Crocker et al. 2011).

Given the very low level of star formation, low attenuation and small amount of gas at the centre of M31, little dust emission was expected in the central kiloparsec of M31. Yet when this region was examined in the far-IR (FIR) with *IRAS* (Habing et al. 1984), *Infrared Space Observatory* (*ISO*; Haas et al. 1998) and *Spitzer* (Gordon et al. 2006), emission at wavelengths greater than 60 μm was clearly seen, indicating the presence of warm dust. In nearby ETGs, low levels of warm dust are also being detected, with Smith et al. (2012) finding dust emission in 24 per cent of ellipticals and 62 per cent of S0s in the *Herschel* Reference Survey (HRS). While M_{dust}/M_* is far lower in spheroids than in discs, the dust appears to be warmer on average than that found in later type galaxies. A similar result was found using *Herschel* in nearby early-type spirals similar to M31 by Engelbracht et al. (2010), with the mean dust temperature of the bulges consistently hotter than the discs in these galaxies. Relatively higher dust temperatures were also found by Rowlands et al. (2012) in the *Herschel*-ATLAS survey of more distant ellipticals. Hence dust, when detected, tends to be in a warmer state in spheroids than that found across the discs of later type galaxies.

Given the high density of stars in bulges, stellar heating is the likeliest explanation for the observed warmer dust temperatures in ETGs. Yet the old stellar ages found in ETGs, and especially in the centre of M31, argue against the standard view that the IR luminosity and warm dust is a direct tracer of star formation (e.g. Kennicutt 1998). Based on the *IRAS* observations and the extremely weak UV observed using the *Astronomical Netherlands Satellite* (*ANS*; Coleman, Wu & Weedman 1980), Habing et al. (1984) put forward the argument that it is the high density of late-type giant stars that provide the strong enough radiation field to heat the dust. Based on *Herschel* Photodetector Array Camera and Spectrometer (PACS) and Spectral and Photometric Imaging Receiver (SPIRE) maps of M31 with unprecedented resolution (Krause et al., in preparation), we follow Habing et al. (1984) and use this high resolution to demonstrate how and by what stellar populations dust is heated in the bulge of this galaxy, and, by proxy, in the spheroids of other inactive ETGs.

We briefly review the *Herschel* data and reduction in Section 2, and discuss the FIR geometry and integrated properties of the M31 bulge in Section 3. In Section 4 we determine and discuss the mean dust temperature across M31 and in the centre, and determine the heating mechanism for the rise in dust temperature in the centre. We finish with the discussion and summary in Sections 5 and 6. The global properties of M31 we assume throughout this paper are listed in Table 1.

Table 1. M31 positional data.[a]

M31 nucleus position[b]	$00^h42^m44\overset{s}{.}35$
(J2000)	$+41^\circ16'08\overset{''}{.}60$
Position angle of major axis	$37\overset{\circ}{.}7$
Inclination	75°
Distance[c]	780 ± 40 kpc[d]
Distance modulus	24.46

[a]Based on NASA/IPAC Extragalactic Database (NED) and references where given.
[b]Evans et al. (2010), and verified in *Spitzer* IRAC 3.6-μm image.
[c]Stanek & Garnavich (1998), Rich et al. (2005), see also NED for other determinations.
[d]1 arcmin = 227 ± 12 pc along major axis.

2 DATA AND REDUCTION

The M31 *Herschel* data and their reduction are described and discussed in detail in Krause et al. (in preparation), so we only briefly review the data here.

M31 was imaged in all six *Herschel* photometric bands (PACS 70, 100 and 160 μm, and SPIRE 250, 350 and 500 μm) in slow parallel mode for a total time of $\sim$24 h. The images extend for $\sim3^\circ \times 1^\circ$, centred slightly off-nucleus [at the position angle (PA) given in Table 1], covering the main stellar disc of Andromeda, including the 10-kpc ring.

All images were reduced to level one using HIPE v6.0, and then used SCANAMORPHOS v12.0 (Roussel 2012) to produce the final images. As HIPE v6.0 was used, we converted the PACS images from flight model (FM), 5 to FM, 6 by dividing by the factors listed in PACS Photometer Point Source Flux Calibration Report v1.0, which are 1.119 (70 μm), 1.151 (100 μm) and 1.174 (160 μm) for the three PACS photometer bands, respectively. All images were converted to MJy sr^{-1}. Based on SPIRE Observers' manual v2.4,[1] we used beam areas of 423 arcsec^2 (250 μm), 751 arcsec^2 (350 μm) and 1587 arcsec^2 (500 μm) for the three SPIRE bands, respectively, to convert from Jy beam^{-1} to MJy sr^{-1}.

The mean full width at half-maximum (FWHM) of the PACS and SPIRE point response functions/beams are $\sim$5.6 arcsec (70 μm), $\sim$6.8 arcsec (100 μm), $\sim$11.4 arcsec (160 μm), 18.2 arcsec

[1] http://herschel.esac.esa.int/Docs/SPIRE/html/spire_om.html

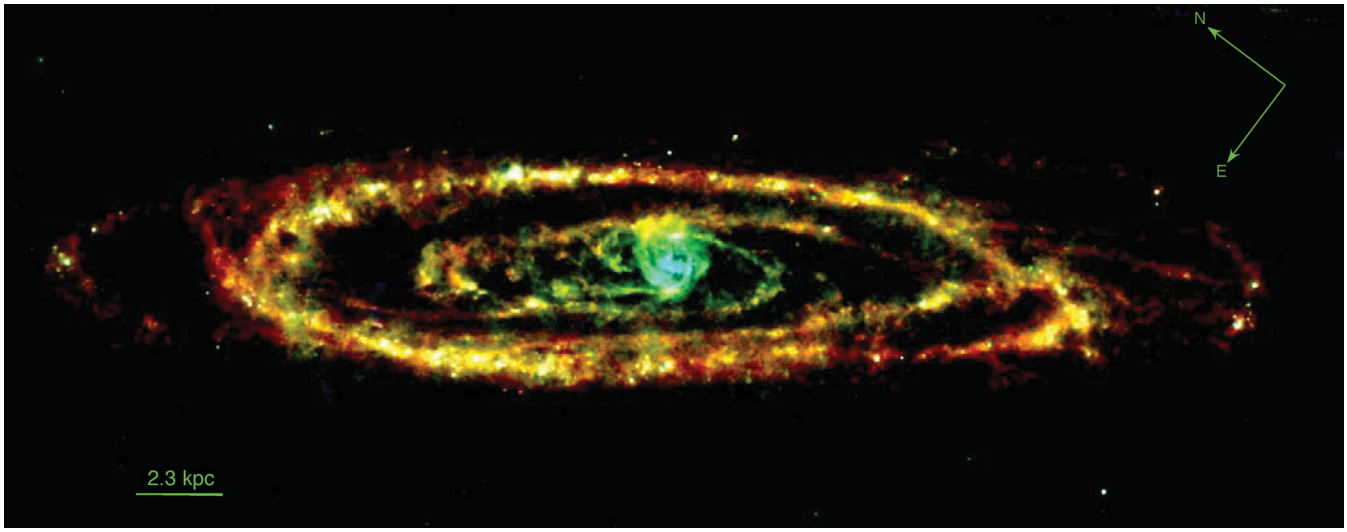

Figure 1. FIR image of Andromeda using the *Herschel* bands showing PACS 70 μm (blue), PACS 100 μm (green) and SPIRE 250 μm (red), all convolved to SPIRE 250 μm resolution (from Krause et al., in preparation). All three bands have the same square root scaling from 10 to 150 MJy sr^{-1}. The angular scale of the image is shown by the 2.3 kpc (10 arcmin) bar in the lower left.

(250 μm), 24.9 arcsec (350 μm) and 36.3 arcsec (500 μm), respectively, for the 20 arcsec s^{-1} scans used here (for full details of the correct point spread functions (PSFs) and beams, see the PACS[2] and SPIRE[1] Observer manuals). The actual images use pixels sizes of 1 arcsec for all PACS bands and 6, 10 and 14 arcsec for the respective SPIRE bands. When comparing bands, we convert all bands to the lowest resolution and pixel size using the convolution kernels provided by Aniano et al. (2011).

For all bands we have measured the noise and background as discussed in Krause et al. (in preparation). The 'background' in the images is a combination of both Galactic foreground and background galaxies, and is significant only in the SPIRE images. For simplicity, a uniform background in each band was assumed and subtracted from the image.

The measured noise for each band in the original images is 3.17 MJy sr^{-1} (70 μm), 3.23 MJy sr^{-1} (100 μm), 2.29 MJy sr^{-1} (160 μm), 0.68 MJy sr^{-1} (250 μm), 0.46 MJy sr^{-1} (350 μm) and 0.20 MJy sr^{-1} (500 μm). When convolved and binned to lower resolutions, the noise per resolution element in each band is obviously reduced, with the effective resolution driven by the longest wavelength (e.g. 36.3 arcsec FWHM and 14 arcsec pixels at the 500 μm resolution).

3 THE BULGE OF M31: STARS, DUST AND GAS

3.1 The FIR emission in Andromeda

In Fig. 1 we show a red–green–blue (RGB) image of the full disc of Andromeda using the PACS 70 μm, PACS 100 μm and SPIRE 250 μm bands. One of the things that stands out in this image, apart from the dusty ring, is the blue centre of the IR map, indicating a distinct rise in dust temperature towards the centre of M31.

The central kiloparsec bulge region [hereafter referring to a circular aperture of radius 4.405 arcmin (1 kpc), centred on the stellar peak defined in Table 1] is relatively weak in the SPIRE 250-μm band compared to the extended disc and star-forming ring, but shows a relative excess in the PACS 70-μm band. The FIR emission in this central region appears more circular and shows a spiral-like pattern within.

3.2 The correlation of dust and gas

The spiral pattern can be seen in finer detail with Fig. 2, where we show the PACS 70 μm and SPIRE 250 μm contours overlaid on the Hα image of the central kiloparsec from Devereux et al. (1994). As demonstrated by Li et al. (2009) using *Spitzer* data (particularly their figs 6 and 8), the IR emission follows well the morphology of the Hα emission. The correspondence is not linear between the Hα and the two *Herschel* bands, with offsets between the Hα peaks and IR peaks, but in general the same barred spiral pattern is seen. The two *Herschel* bands match very well with each other within the inner 0.5 kpc (2.2 arcmin) radius, but outside this the correspondence becomes weaker as the dust becomes cooler, and the PACS 70 μm emission merges with the noise. To the north-west and south-east of the image in Fig. 2(b) we can see the contribution of the disc appearing at the SPIRE 250 μm wavelengths.

The correspondence of the dust and ionized gas emission together suggest that the dust is associated with the gas and also likely to be in the same lower inclination thin disc spiral (Jacoby, Ford & Ciardullo 1985; Ciardullo et al. 1988). The offset between the peaks in the Hα and the IR emission indicates the presence of cooler, denser gas associated with the dust, that is still too low in column density to be observed in H I or CO, with the weak and non-detections in CO of several higher attenuation regions in the centre by Melchior et al. (2000) and Melchior & Combes (2011) supporting this. As the gas emission indicates that most of the gas is in a diffuse state, and attenuation maps show an, on average, extremely low attenuation, it is clear that the dust is likely to be optically thin to a significant amount of the radiation from the bulge stars.

3.3 The spectral energy distribution of the bulge

The low optical depth in the centre of M31 is also made clear by the full UV–IR SED in the central kiloparsec, which is illustrated

[2] http://herschel.esac.esa.int/Docs/PACS/html/pacs_om.html

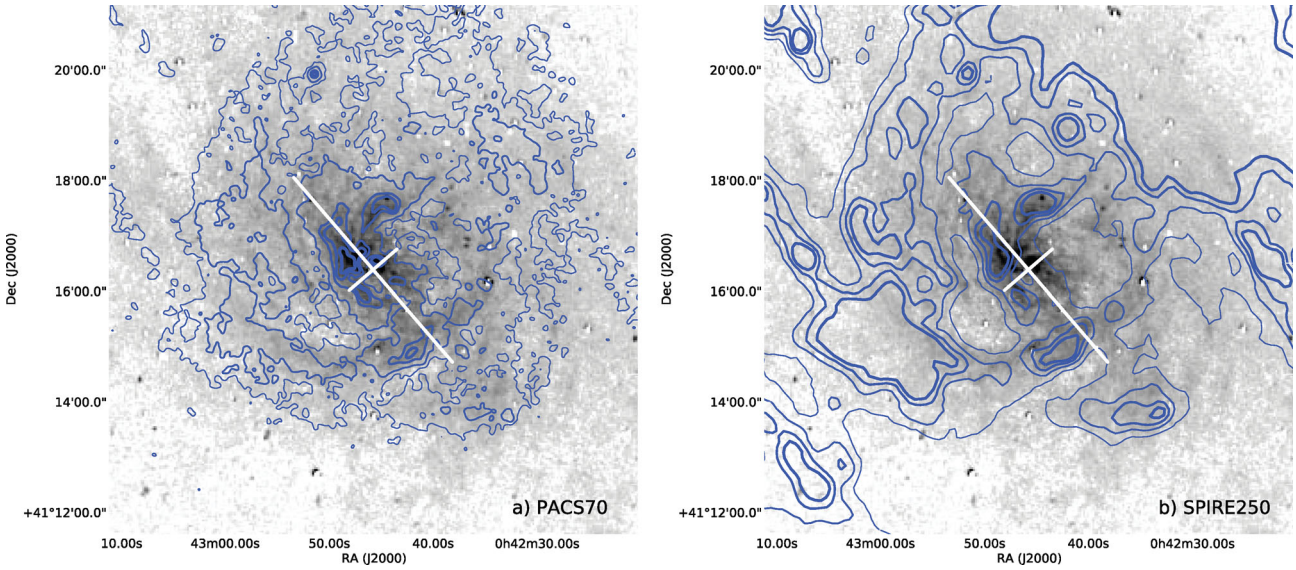

Figure 2. Continuum-subtracted Hα + [N II] narrow-band image of the central kiloparsec of M31 (grey-scale) from Devereux et al. (1994) overlaid with contours from PACS 70 μm (left) and SPIRE 250 μm (right) imaging. In both images the Hα has a square root stretch, and the centre is marked by a cross of 1 kpc length along both the major (4.4 arcmin) and minor axis (1.14 arcmin), assuming the inclination of M31 given in Table 1. For the PACS 70-μm contours, the levels are 15, 30, 70 and 100 MJy sr^{-1}, while for the SPIRE 250-μm contours, the levels are 10, 15, 20 and 25 MJy sr^{-1}, each indicated by an increasing thickness.

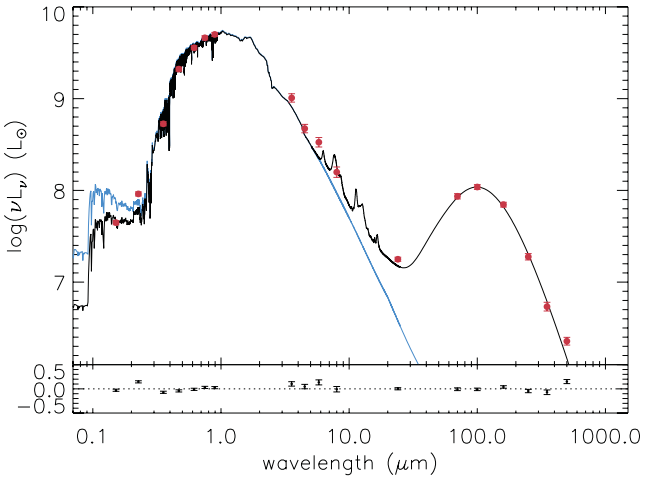

Figure 3. The SED of the central kpc region of Andromeda, measured within a circle of 1 kpc (4.405 arcmin) radius from the centre. The fluxes (*GALEX* FUV and NUV, SDSS *u*, *g*, *r*, *i* and *z*, *Spitzer* IRAC and MIPS24, and all six *Herschel* bands) within this aperture are marked by the red points, with the error bars including calibration, sky and noise uncertainties. The black curve shows the best-fitting model SED from the SED fitting code MAGPHYS (da Cunha, Charlot & Elbaz 2008), while the blue curve shows the corresponding unattenuated stellar SED from the same model. Below the model SED, the residuals between the observed data and models are shown, with $|\log(L_{\rm obs}/L_{\rm mod})| < 0.1$ dex for all wavelengths except for SPIRE 500 μm, where the observed flux is under predicted by ∼30 per cent.

in Fig. 3, drawing on data from the *Galaxy Evolution Explorer* (*GALEX*; Gil de Paz et al. 2007), Sloan Digital Sky Survey (SDSS; Aihara et al. 2011), *Spitzer* Infrared Array Camera (IRAC; Barmby et al. 2006) and Multiband Imaging Photometer for *Spitzer* (MIPS; Gordon et al. 2006), and now *Herschel*. Overlaid on the observed data is the best fit from the SED fitting code MAGPHYS[3] (da Cunha et al. 2008) (black curve) and its implied unattenuated stellar emission (blue curve). For this model fit we created a new stellar library using the original Bruzual & Charlot (2003) code and the same star formation histories as in da Cunha et al. (2008) but excluding all models which were formed less than 6 Gyr ago ($t_{\rm g} < 6$ Gyr; see da Cunha et al. 2008, specifically section 3.1.1), based on previous estimates for the mean stellar age of the bulge of M31 (see Section 1, and e.g. Davidge et al. 2005; Olsen et al. 2006). The MAGPHYS model fit returns a stellar mass within this 1-kpc radius of $\log(M_\star/{\rm M}_\odot) = 10.01 \pm 0.01$, and an unattenuated stellar luminosity of $\sim 10^{9.9}\,{\rm L}_\odot$. The dust luminosity of the M31 centre is $\sim 10^{8.3}\,{\rm L}_\odot$, with MAGPHYS determining a total dust mass of only $\log(M_{\rm dust}/{\rm M}_\odot) = 5.17 \pm 0.05$.

As stated in the Introduction, the $10^{10}\,{\rm M}_\odot$ stellar mass of the bulge makes it a significant fraction (∼30 per cent) of the total stellar mass of M31 (Geehan et al. 2006). The optical–UV colours clearly reveal the old stellar age of the bulge, with NUV $- r \approx 5.0$. These colours lead to an extremely low estimated specific star formation rate (sSFR) from the model, with sSFR $< 0.01\,{\rm Gyr}^{-1}$ (SFR $< 10^{-2}\,{\rm M}_\odot$), in agreement with the lack of young stars observed in the bulge of M31. (Davidge et al. 2005; Olsen et al. 2006; Rosenfield et al. 2012).

It should be noted that the values here for the dust mass and luminosity in the central kiloparsec are likely upper limits for the dust in the bulge, as even at these small radii, some fraction of the IR emission still arises from the disc in the foreground and background due to the high inclination of Andromeda. This contribution of the disc infrared emission may also explain the weak UV (<0.25 μm) excess observed in the unattenuated spectrum of the best-fitting MAGPHYS model relative to the observed SED. To explain the observed IR SED, the MAGPHYS model finds a small component of

[3] www.iap.fr/magphys

buried young stars necessary. This component is small (as demonstrated by the low sSFR), and cannot be associated with the bulge (as the high-resolution observations have shown), but still contributes significantly to the unattenuated UV.

The total attenuation in the diffuse ISM is extremely low, as can be seen in the differences between the black and blue curves, with the model finding an attenuation in the diffuse ISM of only $\tau_V \sim 0.03$. The low value of attenuation measured from the SED matches that observed in *B*-band attenuation maps (Melchior et al. 2000), and is a result of a very low dust column, with the SED fit returning an average dust column density of only $\sim 4.5 \times 10^4\,M_\odot\,\mathrm{kpc}^{-2}$ in the central region.

In contrast to the stellar mass, the bulge contributes little to the total dust mass in M31. At larger radii, emission from the disc of M31 along the minor axis overlaps with (and dominates over) the dust emission from the bulge. Fits to the integrated IR SED of the Andromeda galaxy (within a 21.5-kpc aperture; Krause et al., in preparation), using both the Draine & Li (2007) and da Cunha et al. (2008) models, reveal that the dust mass in the inner 2 kpc only contributes ∼0.5 per cent to the total dust mass of M31. However, the central 1 kpc contributes a 10 times larger fraction (i.e. ∼5 per cent) to the total IR luminosity of M31, because of the relatively warmer dust emission. We can quantify the temperature of this dust in the bulge and in the rest of M31 by fitting simple modified blackbodies.

4 THE DUST HEATING IN THE M31 BULGE

4.1 Simple modified blackbodies

We now convert the spatially resolved thermal-IR SEDs into dust temperatures, describing the emission locally with a single dust temperature, T_d. While a simplification, this method returns a reasonable estimate for the mean, luminosity-weighted temperature of the dust.

We do this by using a simple modified blackbody:

$$S_\nu = N_d \kappa_{\nu 0} B_\nu(T_d) \left(\frac{\nu}{\nu_0}\right)^\beta, \quad (1)$$

where the dust surface brightness, S_ν, is proportional to the Planck function for the given dust temperature, $B_\nu(T_d)$, modified by the dust emissivity, which is assumed to be a power-law function of frequency, $\kappa_{\nu 0}(\nu/\nu_0)^\beta$. At a given dust temperature this is then simply multiplied by the dust column density, N_d, to yield the surface brightness.

The power-law function is a reasonable approximation for the dust emissivity (see e.g. Hildebrand 1983; Draine 2003), with the galactic diffuse ISM well fit by an emissivity index of $\beta = 2$ (Draine & Lee 1984). While a mean temperature for the dust can be determined, in reality there will be a range of temperatures along the lines-of-sight due to both a distribution of grain sizes and heating radiation fields (see e.g. Draine & Li 2007). This simplified modelling foremost reflects a physically motivated conversion of the FIR colours into the three parameters returned by the fitting procedure: T_d, β and $N_d \kappa_{\nu 0}$. We refer to Shetty et al. (2009a,b) for a more detailed description of the issues and uncertainties in using simple modified blackbodies for integrated IR data.

We fit the modified blackbody to the 100–500 μm *Herschel* bands at the 500 μm resolution. We do not include the PACS 70-μm data due to the lower signal-to-noise ratio (S/N) across the M31 image, and as we expect the emission at these wavelengths to have a significant contribution from stochastically heated dust grains. We limit our fitting to all pixels with S/N > 5 in all five bands, which in practice is limited predominantly by the PACS 100-μm band. To fit the simple modified blackbody to the data, we assume a uniform, bounded prior grid for all three parameters, compute the χ^2 goodness of fit for every model parameter set *j*,

$$\chi_j^2 = \sum_\nu \left(\frac{S_{\nu,\mathrm{obs}} - S_{\nu,j}}{\sigma_\nu}\right)^2, \quad (2)$$

where $S_{\nu,\mathrm{obs}}$ and σ_ν are the observed surface brightness and observational uncertainty for the band ν, respectively, and $S_{\nu,j}$ is the model flux for parameter set, *j*, determined from equation (1). The bounds for dust temperature and emissivity were $5 < T_d < 50$ and $0.5 < \beta < 3.5$, respectively. We then determine the probability for each parameter set assuming a Gaussian distribution, $\exp(-\chi_j^2/2)$, and marginalize over the other parameters to determine the probability distribution function (PDF) for each parameter, e.g. T_d. An examination of the PDF for T_d in several pixels shows a symmetric Gaussian distribution (as can be seen in the symmetric uncertainties in Fig. 5), providing justification for our assumed Gaussian uncertainties for the parameters.

4.2 The dust temperature across M31

We performed this fit for every 14 arcsec pixel in the M31 IR data that laid above our S/N cut, with the resulting image for the dust temperature shown in Fig. 4. Pixels which fall below our S/N cut are shown as white, with the dust temperature (K) shown by the colour, as indicated by the colour bar at the bottom of the image. Note that within 2 kpc, almost all pixels have sufficient S/N. The median temperature across the image is 17 K, close to MIPS-based disc temperature of 18 ± 1 K determined by Tabatabaei & Berkhuijsen (2010). The uncertainties (half the 16–84 percentiles, or 1σ if the uncertainties are Gaussian) range from 5 to 15 per cent, with the largest uncertainties in regions at the lowest S/N and the central kiloparsec. The median uncertainty is ∼6 per cent (∼1 K) dominated by the emission in the dusty, star-forming ring seen in *GALEX* and FIR images (e.g. Thilker et al. 2005).

Two things stand out in this temperature map: the almost constant temperature in the disc of M31, with $T_d = 17 \pm 1$ K, and the strong temperature increase in the central ∼2 kpc. The temperature in the 10-kpc ring of M31 is clearly not exactly constant, with warm spots occurring throughout the ring. These warm spots correspond with the locations of H II regions in the disc as determined by Hα images (cf. the Hα maps of Devereux et al. 1994; Azimlu, Marciniak & Barmby 2011).

4.3 The radial dust temperature

The central dust temperature rise is more clearly quantified by taking the median SED in radial bins. To do so we determined the median flux in all bands in radial bins of 230 pc (using elliptical annuli with a PA = 37°.7 and axis ratio of 0.26), and determined the PDFs for all three parameters for each radial bin. The resulting temperature variation with radius is shown in Fig. 5, with the 16–84 percentiles marked by the error bars. This plot clearly shows the marked increase in dust temperature in the inner 2 kpc from the median disc dust temperature of T_d = 16–17 K. The peak in dust temperature at the centre of ∼35 K is similar to the dust temperature of T_d = 33 K determined by Soifer et al. (1986) for the central 4 arcmin, using *IRAS* data and assuming a power-law emissivity of $\beta = 2$. Similarly, Habing et al. (1984) found 34 K (using $\beta = 1$)

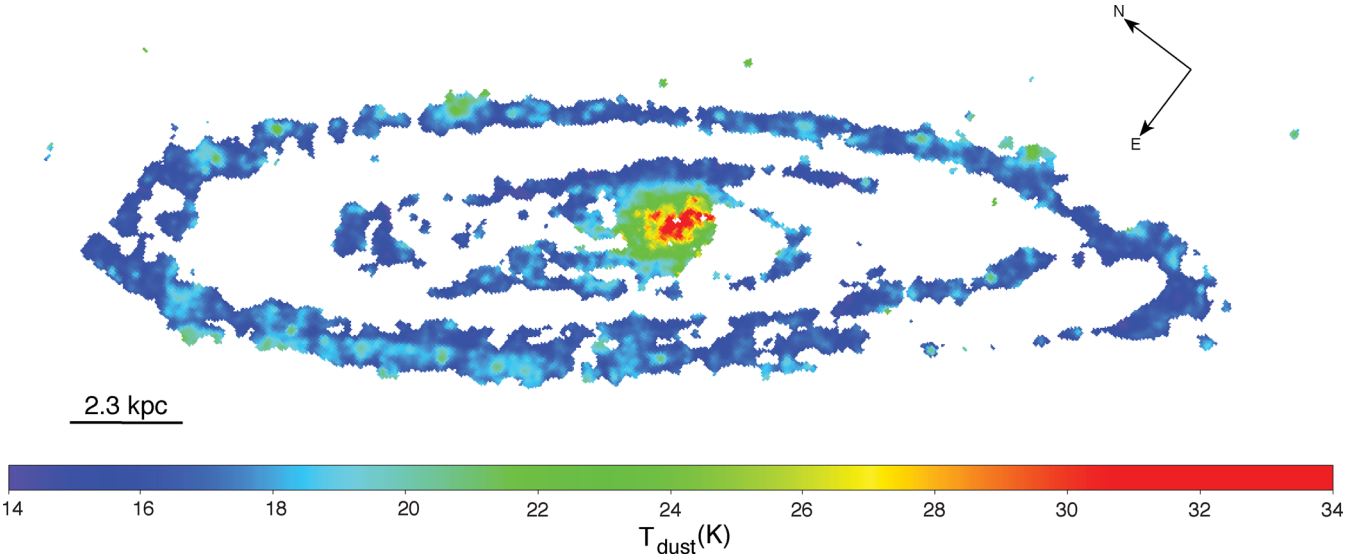

Figure 4. Effective dust temperature map of M31, determined from a single modified blackbody fit to each matched pixel of the PACS 100, 160 μm and SPIRE 250, 350 and 500 μm bands, with all bands convolved to the SPIRE 500 μm PSF and resolution (as described in Sections 4.1 and 4.2). The median temperature is 17 K, and is dominated by the emission in the ring, while the highest temperature is reached in the nuclear region, as can be seen by the clear gradient in the figure. The median uncertainty is ∼1 K or ∼6 per cent.

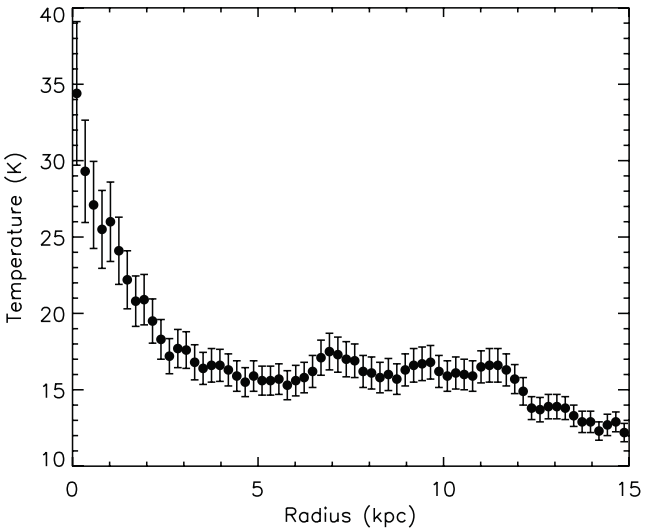

Figure 5. Radial variation of mean temperature in M31. The temperature is determined by fitting the median flux in all bands in radial bins of 230 pc width using elliptical annuli. The error bars show the 16–84 percentiles of marginalized PDFs.

for approximately the same central region and same data. As these works use apertures of 4-arcmin diameter, to define the centre, these temperatures represent an average of the inner ∼0.35–0.45 kpc and thus are remarkably close to our determined value. As these fits are based on only the *IRAS* 60 and 100 μm bands, and thus biased to the warmer dust temperatures due to the shorter wavelengths, the similarity in temperatures suggests that a single, warm component of dust dominates the IR SED in the centre. This is supported by the similarity of the PACS 70-μm flux and the model flux in the central kpc, even though not actually used to determine the fit.

In addition to giving access to the full IR SED, and thus a better measure of dust temperature, the higher resolution of *Herschel* enables us to see the steep gradient in temperature from the disc to the centre. This difference between the bulge and disc dust temperature in M31 agrees with what Engelbracht et al. (2010) found for the KINGFISH sample of nearby galaxies (Kennicutt et al. 2011). Engelbracht et al. (2010) found that the ratio of the central to disc dust temperature was greater than 1 across their sample, and increased with increasingly earlier types (see e.g. their fig. 3).

The emissivity, β, determined from these fits has a large uncertainty across M31, and is consistent with $\beta = 2$ at all radii. Given this, we created a higher resolution temperature map using only the 100, 160 and 250 μm bands with the assumption of a constant emissivity of $\beta = 2$. The resulting image of the central region is shown in Fig. 6, where the central kiloparsec region is marked as a black circle and the median uncertainty is 0.75 K. Interestingly,

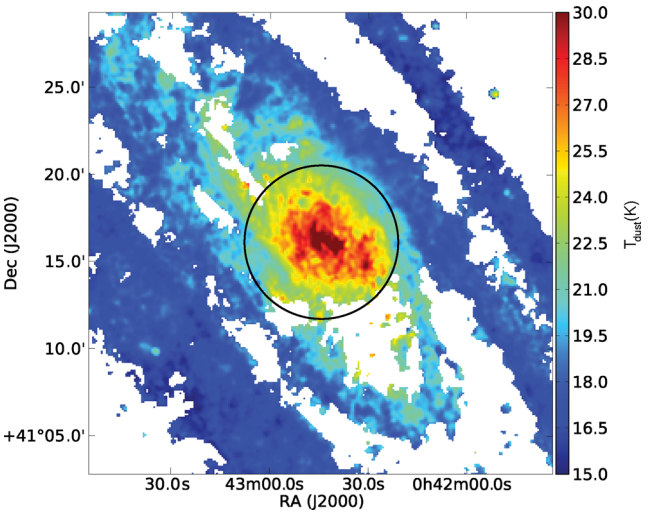

Figure 6. Effective dust temperature map of the central region of M31, determined from a single modified blackbody fit to each matched 6 arcsec pixel of the convolved PACS 100, 160 μm and SPIRE 250 μm bands, assuming a constant emissivity of $\beta = 2.0$. The black circle outlines the central kiloparsec region.

while more structure in the temperature distribution in the centre is seen due to the higher resolution, the overall temperature gradient in the centre still dominates the image. The steeper gradient in dust temperature along the minor axis arises from the mixture of disc dust emission with that from the bulge, leading to an overall lower average dust temperature in these regions. The fine scale structure is likely due to the distribution of the diffuse gas and dust as seen in Fig. 2.

4.4 The heating mechanism of the bulge dust

The clear temperature increase in the central regions of M31 as seen in Fig. 5 is interesting as it closely corresponds with the stellar light distribution as traced by the near-IR emission, suggesting that the heating of the dust and bulge are linked. As Li et al. (2009) demonstrated (particularly their fig. 3c), both the Hα and diffuse X-ray emission also increase towards the centre in the same manner as the stellar light. However, with the resolution offered by *Herschel* we can begin to understand the heating of the dust in the bulge of M31, and by proxy in the bulges of early-type spirals and in ETGs.

4.4.1 Potential heating sources

In principle, one possibility for heating the dust is a low level of star formation, buried amongst the dust and bulge stars. However, high-resolution observations by *Hubble Space Telescope* (*HST*) show that no OB stars are apparent throughout the bulge (e.g. Brown et al. 1998; Rosenfield et al. 2012), and no regions of high enough attenuation to bury such potential star formation are observed (Melchior et al. 2000). Also, the observed emission-line ratios in the ionized gas (e.g. [N II]/Hα) argue against young stars being the dominant heating mechanism (Ciardullo et al. 1988; Saglia et al. 2010).

As the supermassive black hole at the centre of M31 (dubbed M31*) is quiescent (Li et al. 2011), heating by an active galactic nucleus (AGN) radiation field can be discounted. In addition, the radial profile of dust temperature is incompatible with a dominant central source heating, as shown in the following section.

Collisional heating of the dust by the hot 10^6 K X-ray gas at the centre of M31 (Li & Wang 2007) is another possibility (see e.g. Voit 1991; Natale et al. 2010). However, the association of the dust with the Hα emission and the weak detection of CO in regions of higher attenuation (discussed in Section 3.2) indicate that the dust is in a denser medium, and not predominantly associated with the X-ray gas itself. Likewise, the total energy in the diffuse X-ray gas is insufficient to fully explain the Hα emission, and thus is unlikely to heat the dust either (Li et al. 2009). Thus, while this may contribute to the emission, it is insufficient to explain the majority of the hot dust emission.

4.4.2 Bulge star heating

This leaves the high stellar density of old stars at the centre as the dominant heating mechanism of the dust in the bulge of M31, as originally suggested by Habing et al. (1984). By comparing the stellar light distribution for the bulge against the distribution of temperatures in the central kiloparsec, we can now demonstrate the link between the heating of dust by the bulge and the dust emission. In the case of a simple steady-state temperature, grain cooling balances the dust heating, and the grain temperature is then proportional to (as shown in e.g. Draine 2011, particularly equations 24.17 and 24.18)

$$T_{\rm d} = \left(\frac{h\nu_0}{k_{\rm B}}\right)^{\beta/(4+\beta)} \left[\frac{\pi^4 \langle Q_{\rm abs}\rangle_\star c}{60\Gamma(4+\beta)\zeta(4+\beta)Q_0\sigma}\right]^{1/(4+\beta)} U_*^{1/(4+\beta)}, \quad (3)$$

where Q_0 and $\langle Q_{\rm abs}\rangle_\star$ are the dust absorption cross-section at the reference frequency ν_0 and averaged across the heating spectrum (equation 24.2 in Draine 2011), respectively, Γ and ζ are the Gamma and Riemann zeta functions and U_* is the heating stellar radiation field density. In the simple assumption where the emissivity slope is constant at $\beta = 2$, this reduces to

$$T_{\rm d} = \left(\frac{21h^2c}{160\pi^2 k_{\rm B}^2\sigma}\right)^{1/6} \left(\langle Q_{\rm abs}\rangle_{\star,0}\nu_0^2 U_*\right)^{1/6}, \quad (4)$$

where $\langle Q_{\rm abs}\rangle_{\star,0}$ is the spectrally averaged dust absorption cross-section normalized at ν_0. Using a reference wavelength of $\lambda_0 = 100\,\mu$m and the unattenuated SED determined in Section 3.3, $\langle Q_{\rm abs}\rangle_{\star,0} \sim 197$ for a Milky Way dust model with $R_{\rm V} = 3.1$[4] (at $\lambda_0 = 250\,\mu$m, $\langle Q_{\rm abs}\rangle_{\star,0}$ is approximately $(2.5)^2$ larger; Draine 2003).

We can estimate the stellar radiation field heating the dust with a few simple assumptions: (1) the dust is in a thin disc at the centre of M31, (2) is optically thin to the dominant heating radiation, (3) the bulge stellar mass is spherically distributed and (4) has constant colours and stellar population. The first assumption is based on the findings given in Section 3.2, where the correlation of ionized gas and dust suggests a thin disc geometry. The measured opacity in the bulge of M31 is low, as shown by Melchior et al. (2000), as is the average dust column of $\sim 4.5 \times 10^4\,{\rm M}_\odot\,{\rm kpc}^{-2}$ (see Section 3.3), thus the assumption of optically thin dust is not unreasonable. As for the third assumption, the bulge of M31 has already been shown to be non-symmetric, displaying a boxy structure and possibly even different PA and inclination angle to the disc (e.g. Courteau et al. 2011). However, a simple spherical approximation for the bulge with a constant mass-to-light ratio can actually reasonably well reproduce the stellar light profile, as shown by Geehan et al. (2006). The NIR colours are close to constant as shown in fig. 1 in Courteau et al. (2011), but the UV colour, however, does show a gradient (see e.g. fig. 3 in Thilker et al. 2005). While some of this may arise from a gradient in attenuation, there exists also radial gradients in the UV-emitting stellar populations (Rosenfield et al. 2012) that may affect our assumptions (though the follow section argues against this).

As shown in Appendix A, given these assumptions, using the model for the bulge profile from Geehan et al. (2006) and the integrated unattenuated stellar luminosity from Section 3.3, the bulge interstellar radiation field (ISRF) heating the dust is

$$U_*(r) = \frac{3.66\times10^{-11}}{(r/{\rm kpc})}\int_0^\infty \frac{\ln\left(\frac{r/r_{\rm b}+x}{|r/r_{\rm b}-x|}\right)}{(1+x)^3}{\rm d}x\ {\rm erg\,cm^{-3}}, \quad (5)$$

at a radius r (in kiloparsec), and a bulge scale radius of $r_{\rm b} = 0.61$ kpc.

From equations (4) and (5), we can then determine the expected dust temperature (given the above assumptions) as a function of spherical radius. For an infinitely thin disc, located in the plane of M31, we can equate the dust temperature in spherical coordinates with that in cylindrical (i.e. $r = R, z = 0$), giving

$$T_{{\rm d},U_*}(R) = 1750\,[U_*(R)]^{1/6}\ {\rm K}, \quad (6)$$

where the factor 1750 arises from using the Milky Way dust model described above for $\langle Q_{\rm abs}\rangle_{\star,0}$, and U_* is in erg cm^{-3} as in equation (5).

[4] Available from http://www.astro.princeton.edu/~draine/dust/dustmix.html

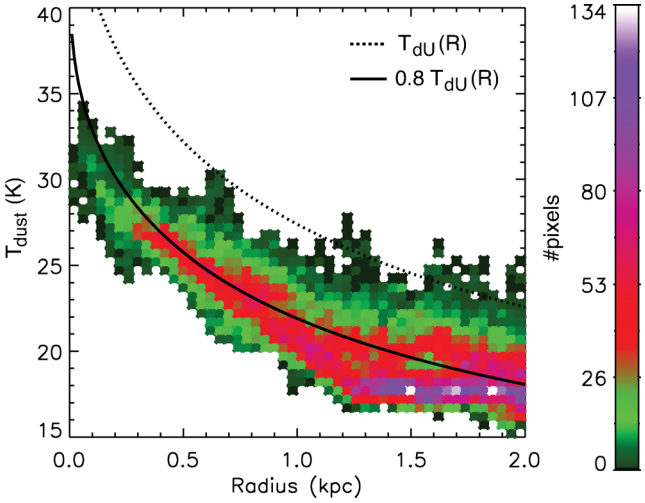

Figure 7. The distribution of dust temperatures within the inner 2 kpc (530 arcsec) of M31. The colours show the number density of the 6 arcsec pixels from Fig. 6 in terms of ($T_{\rm d}$) and circular radius, as labelled by the colour bar to the right. Overlaid on this are two curves showing expected heating as based on the determined bulge ISRF. The dotted and solid curves show, respectively, the expected dust temperature distribution, $T_{{\rm d},U_*}(R)$, from equation (6) and the same $T_{{\rm d},U_*}(R)$ scaled by 0.8.

In Fig. 7 we show the distribution of the 6 arcsec pixels from the dust map in Fig. 6 in terms of the dust temperatures with distance from the centre, based on our simple circular radius. Overlaid on this distribution are two curves. The expected dust heating distribution, $T_{{\rm d},U_*}(R)$, as given by equation (6), is shown by the dotted curve. As is clear from the figure, this is in excess of the observed temperature in M31's bulge. The solid curve shows the same $T_{{\rm d},U_*}(R)$, however, multiplied by a factor of 0.8. This brings it in agreement with the observed temperature distribution except at radii larger than $\sim$1.2 kpc. The first thing to take from these two curves is that the bulge provides a more than sufficient ISRF (ISRF$_{\rm b}$) to heat the dust, with expected temperatures in excess of that observed. However, importantly, the observed gradient in temperatures matches that expected from heating the bulge. This leaves the question, why is the expected temperature distribution in excess of that observed?

There are several possibilities given our simple assumptions. One possible explanation is suggested by the flattening of the $T_{\rm dust}$ pixel distribution in Fig. 7 at radii $>$1.3 kpc. This flattening is most likely due to the increasing disc contribution to the IR at these radii, which acts to lower the mean line-of-sight dust temperature. This is approximately the radius where the stellar mass distribution, and therefore light distribution, becomes disc dominated (see e.g. Geehan et al. 2006; Courteau et al. 2011), and thus disc dust is likely also dominating the determined dust temperature. As discussed in Section 4.2 and shown in Fig. 4, the mean dust temperature across the disc is $\sim$17 K, which is also where the pixel distribution flattens to in Fig. 7. Fig. 6 also gives some indication of the disc contribution to the bulge temperature, as there is clearly a flatter gradient of temperatures along the major axis as compared to the minor axis, which should have a greater contribution of disc dust due to the high inclination of M31. However, an examination of the observed IR SED within the central kiloparsec indicates that it is well described by a single blackbody, as mentioned in Section 4.3. As a confirmation we also fitted the pixel SEDs in the central region with a combination of two modified blackbodies. For both blackbodies, we assumed an emissivity of $\beta = 2$, and let the temperature of the first component free, and that of the second, cooler component constrained to 17 K. A simple fit found that the central kpc region is dominated by the warmer component, whose temperature distribution is almost indistinguishable from Fig. 7. Thus, while it must occur at radii $>$1 kpc, the contribution of the disc cannot explain the offset between the theoretical curve and the observational-based temperature.

Another possibility is that the dust in the bulge is not Milky Way like, and our assumed $\langle Q_{\rm abs}\rangle_{\star,0}$ is incorrect. For example, if we assume a Milky Way model of dust, but with $R_{\rm V} = 5.5$ (using the Weingartner & Draine 2001 model opacity), $\langle Q_{\rm abs}\rangle_{\star,0}$ reduces to $\sim$155 (normalized at $\lambda_0 = 100\,\mu$m, as above). Such a possibility is reasonable, given that the extreme environs of the bulge may act to alter the dust size distribution, destroying small grains leading to a flatter opacity. However, given the index of 1/6 in equation (4), the offset in temperature requires a significant change in dust opacity if this alone causes this offset. Similarly, our estimate of U_* is also likely incorrect given that the bulge is not spherical (Courteau et al. 2011), and the dust is not in a perfectly thin disc. However, the index of 1/6 again requires our U_* to be overestimated by approximately an order of magnitude if it alone is incorrect.

More likely, it is a combination of these, plus the possibility of some self-shielding by dust (which acts to reduce the U_* seen by the dust), which lead to the difference between the theoretical temperature distribution and that determined from the modified blackbody fit to the data. Yet it should still be noted, that these are all needed to reduce the theoretical heating to that observed. The bulge stellar radiation field provides more than sufficient energy to heat the warm dust at the centre of M31.

As a final check that the bulge stars are dominating the heating, we can apply the same methodology and reasoning as used for equation (4), but assuming that the radiation field heating the dust arises from a central point source (i.e. AGN or nuclear star cluster), meaning that $U \propto r^2$. However, when $T_{{\rm d},U_*}(R)$ is determined for this radiation field (similar to equation 6), the slope does not show the same form as in Fig. 7, demonstrating that the heating radiation field must be extended. Even allowing for a greater contribution of the disc emission to approximate the observed slope, to match the point source $T_{{\rm d},U_*}(R)$ to the measured $T_{\rm d}$, requires a central luminosity that would be obvious in the optical (or X-ray) emission, which is discounted by observations as already discussed (Li et al. 2009).

4.5 The heating of dust by old stars

While Fig. 7 clearly links the bulge with the dust emission, it does not reveal what exactly is heating the dust. Typically, due to the steep wavelength dependence of the dust opacity, the dust IR emission has been associated with UV light and hence star formation. Typically, diffuse dust is considered to be heated by a local ISRF or scaling thereof (see e.g. Draine & Li 2007). As this ISRF is typically based on the local ISRF of Mathis, Mezger & Panagia (1983), the UV light dominates the heating of dust (e.g. fig. 4 in Mathis et al. 1983), and as the local UV light is dominated by B stars, the diffuse dust emission indirectly traces B stars and thus star formation on longer ($\sim$100 Myr) time-scales. As shown by Thilker et al. (2005), the UV light strongly peaks at the centre of M31. However this UV light in the bulge has been shown to be not associated with star formation, but rather arises from extreme horizontal branch stars (Brown et al. 1998; Rosenfield et al. 2012).

However, while these hot, low-mass stars may be the source of the UV upturn and possibly the Hα emission, they cannot be the dominant heating source of the dust. Based on the *IRAS* and

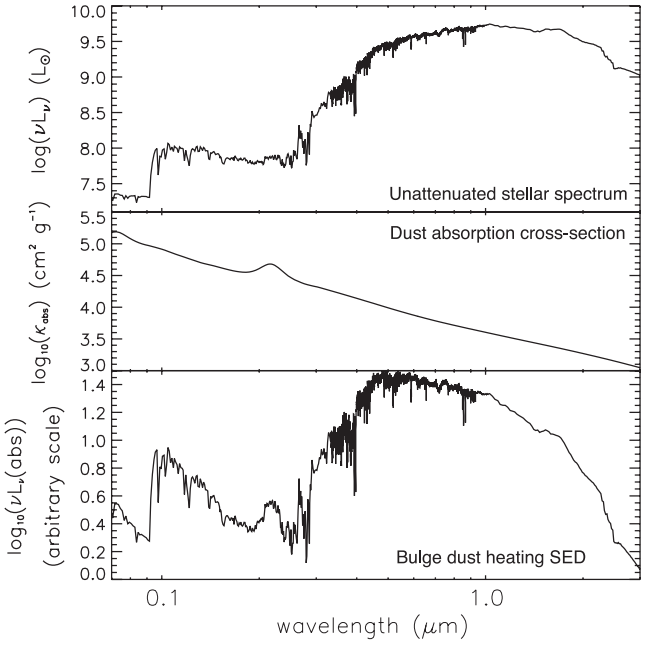

Figure 8. The energy absorbed by diffuse dust in the bulge of M31. The top panel shows the 'unattenuated' bulge UV–NIR SED from the MAGPHYS (da Cunha et al. 2008) model fit to the integrated SED of the central kiloparsec (blue curve in Fig. 3). The middle panel shows the total absorption cross-section per gram of dust for the MW dust model with $R_V = 3.1$ from Draine (2003). The bottom panel shows the product of these, revealing the wavelength distribution of the energy absorbed by dust. The conclusion is that the optical stellar light is the main contributor to the dust heating in the bulge.

ANS observations, Habing et al. (1984) realized that the UV light would not be sufficient to heat the dust, and the heating would be dominated by the $\lambda > 300$ nm light from evolved stars. In Fig. 8, we show three panels that illustrate which radiation heats the dust. In the top panel we take the 'unattenuated SED' from Fig. 3, which is likely an overestimate at $\lambda < 0.25$ μm (see Section 3). The middle panel shows the total dust absorption cross-section per gram of dust for the MW dust model with $R_V = 3.1$ from Draine (2003), as also used in the previous section. By multiplying these together we obtain the amount of energy absorbed per H atom as a function of wavelength (bottom panel). This figure reveals that most of the energy that heats the dust arises from optical photons, not the UV. As the $Q_{abs}(\nu)$ slope is ≈1, the UV–optical slope needs to be <-1 (in frequency) for optical photons to dominate the heating of dust.

As mentioned before, the bottom panel of Fig. 8 most likely overemphasizes the role of UV photons in the heating due to the small UV excess in the model stellar SED (blue curve in Fig. 3). The intrinsic UV emission produced by the evolved stars in the centre of M31 (the so-called UV-upturn observed in ETGs) is well reproduced by the Bruzual & Charlot (2003) code, as shown by a comparison of models with the observed UV colours of ETGs (see specifically fig. 5 in Donas et al. 2007). Even if the model UV is incorrect, the intrinsic UV flux would still need to increase by ∼0.4 dex (or 0.7 dex from the observed value) to be commensurate with the energy deposited in the optical. This lack of UV heating is also clear when the top panel of Fig. 8 is compared with the ISRF of Mathis et al. (1983) (e.g. their fig. 1). When normalized to the peak at ∼1 μm (in both radiation fields), the UV in the IRSF is approximately an order of magnitude greater than that determined in M31.

Furthermore, the hot environment of the circumnuclear region of M31 may destroy the smallest dust grains as discussed in the previous section. The destruction of small grains flattens the slope of $\kappa_{abs}(\nu)$, leading to yet a greater dominance of optical photons in the dust heating. Thus the bulge of M31 is a clear case where the heating of dust is dominated by the light from old stars. This is in stark contrast to typical star-forming galaxies, where the UV from young stars dominates the heating of dust (e.g. Law, Gordon & Misselt 2011). Montalto et al. (2009) had already found with *GALEX–Spitzer* data that the dust in the Andromeda galaxy as a whole appears to be heated mainly by stars a few Gyr old. Habing et al. (1984) already inferred that the bulge of M31 takes this further with heating likely dominated by evolved stars. However, the mean stellar age of the bulge of M31 is >6 Gyr, with some estimates placing the dominant age $\gtrsim$10 Gyr (Davidge et al. 2005; Brown 2009; Saglia et al. 2010), demonstrating that even the oldest stars are able to heat dust. This is a clear cautionary note against using warm IR emission as a direct tracer of star formation, or obscured UV emission.

5 DISCUSSION

As the nearest massive galaxy, the Andromeda galaxy allows us to connect the small-scale physics with the integrated properties of galaxies. The central kiloparsec of M31 actually matches very well many of the observed properties of nearby ETGs. Within a 1 kpc (4.4 arcmin) circular aperture the estimated stellar mass is $\sim 10^{10}$ M$_\odot$, with a very old, red stellar light, estimated to be greater than 10 Gyr old (Saglia et al. 2010). The optical colours of the bulge, e.g. NUV $- r \approx 5.0$, place it well in the realm of gas-poor ETGs (see e.g. Oke & Sandage 1968; Saintonge et al. 2011; Smith et al. 2012).

There is a low level of dust attenuation across the centre, visible in both the difference between the observed and modelled intrinsic SEDs in Fig. 3 and in the A_B map (their fig. 1) of Melchior et al. (2000). This low level of attenuation is a result of the low dust column across the centre and connected to the relatively weak IR emission. The total dust mass within this aperture from the da Cunha et al. (2008) MAGPHYS model is $10^{5.2}$ M$_\odot$, contributing only 0.5 per cent of the total dust mass to M31. However, the bulge contributes ∼5 per cent of the total IR luminosity due to the relatively warm, blue FIR emission. This dust mass results in a very low $M_{dust}/M_\star$ for the bulge, with $\sim 10^{-4.7}$. This actually places the bulge of M31 in a similar regime as the sample of ETGs explored in the HRS (Boselli et al. 2010) in Smith et al. (2012), falling somewhat in between the S0 and E galaxies (see their fig. 8). Similarly, the temperature increase from disc to bulge in M31 follows the trend of having warmer dust in earlier Hubble types, as observed by Engelbracht et al. (2010) in the KINGFISH sample. This trend was also seen by Smith et al. (2012) in the HRS, who found warmer dust in E galaxies than S0, and an overall warm dust temperature for the sample (mean $T_d = 24$ K).

The $M_{gas}/M_\star$ ratio is also very low in the bulge of M31, with little H I and CO detected in the centre. However, ionized gas is seen in Hα and the FIR emission is spatially well correlated with this gas showing a similar lower inclination, barred-spiral pattern as visible in Fig. 2, with the mid-IR emission also following the diffuse Hα morphology (Li et al. 2009). Given this correlation, the Hα emission allows the structure of the dust distribution to be determined (e.g. Jacoby et al. 1985), and indicates that the ISM in the centre, including the dust, is in a thin, spiral disc. The origin of this gas and dust in the centre of M31 is still not known, and

beyond the scope of this work. Li et al. (2009) suggest that the stellar ejecta are more than sufficient to replenish the observed hot gas in M31's centre, and suggest the rest of this matter comes out as a hot, X-ray flow. However, the spiral pattern observed in the bulge does appear to link up with the emission in the disc (Fig. 1), even if it appears to be at a different inclination to the disc.

Given the above similarities using the bulge of M31 as a resolved representative of the spheroids of other ETGs is a reasonable assumption. Based on this and our resolved study of dust heating in the bulge we can extrapolate to infer that a similar heating mechanism for the dust occurs in the majority of ETGs in which dust is detected (i.e. the Smith et al. 2012 sample). While many ETGs do have some AGN activity in the centre, and several, generally with higher gas masses, have observed active star formation (e.g. Crocker et al. 2011), the combination of diffuse, optically thin dust and a strong, diffuse radiation field due to the high stellar density is able to heat dust at the centres of these ETGs to a significantly warmer level than that observed in most stellar discs. This increased dust temperature makes the generally dust poor early types still visible in the recent and ongoing FIR surveys with *Herschel*.

However, the possible contribution of disc dust to the observed IR emission, as derived from the dust temperature offset in Fig. 7, suggests a final cautionary note in this extrapolation. The bulge of M31 lies in a far different environment to typical ETGs, which affects both the observed emission, and the evolution of the ISM in this early-type spheroid.

6 SUMMARY

When observed in the FIR, the bulge of the Andromeda galaxy (M31, NGC 224) stands out as a region of luminous blue emission (i.e. 70 μm bright), surrounded by ring-like red emission from the disc. This corresponds to a peak in the mean dust temperature, $T_{\rm d}$ (Fig. 4). Across the disc of M31, the mean dust temperature is reasonably constant with $T_{\rm d} = 17 \pm 1$ K. However, within the central kiloparsec, the temperature of the dust rapidly increases, reaching $T_{\rm d} \sim 35$ K at the centre, as seen in Fig. 5.

The start of this upturn is also where the bulge begins to dominate the stellar radiation field, clearly indicating that the heating mechanism of this warm dust and the bulge is associated. Heating by either an AGN or gas-grain collisions is discounted by X-ray observations, leaving stellar heating as the likely source. The radial profile of this steep increase in temperature in the inner kiloparsec corresponds well with the temperature slope expected from heating by the diffuse radiation field arising from the bulge stars, suggesting direct link. The theoretical dust temperature based on the diffuse radiation field and our assumptions is actually in excess of that observed, providing more than sufficient heating. This excess suggests the not unreasonable possibilities of different dust properties in the bulge from the standard diffuse dust in the Milky Way and that the dust is likely to be in a clumpy distribution with some self-shielding occurring.

However, even though the bulge of M31 is observed in the UV, no young stars are seen in *HST* observations or spectra (Saglia et al. 2010; Rosenfield et al. 2012), leaving old (>6 Gyr) stars as the dominant heating mechanism. Furthermore, by taking the observed SED of the bulge and standard dust opacity it is clear that it is the red optical light of these old stars that dominates the heating of the warm dust in the centre, as originally suggested by Habing et al. (1984) with the *IRAS* observations.

Together this demonstrates the possibility of heating dust by stars >10 billion years old. This is one of the clearest demonstrations of how IR emission does not always correlate with star formation, a common assumption, but rather is dependent upon the distribution of dust (and associated gas) and the total radiation field, which includes both young and old stars. The bulge of M31 also demonstrates one of the plausible mechanisms for heating the relatively warm dust observed in the centres of early-type spirals, and ETGs.

ACKNOWLEDGMENTS

The authors would like to thank P. Barmby and K. Gordon for providing the *Spitzer* IRAC and MIPS data for M31, respectively. BG would also like to thank R. Shetty, A. Stutz, G. Seidel and G. van der Ven for interesting and helpful discussions. FT acknowledges the support by the DFG via the grant TA 801/1-1. This work made use of the NASA Extragalactic Database, and the IDL astro library routines.

REFERENCES

Aihara H. et al., 2011, ApJS, 193, 29
Aniano G., Draine B. T., Gordon K. D., Sandstrom K., 2011, PASP, 123, 1218
Azimlu M., Marciniak R., Barmby P., 2011, AJ, 142, 139
Barmby P. et al., 2006, ApJ, 650, L45
Boselli A. et al., 2010, PASP, 122, 261
Braun R., Thilker D. A., Walterbos R. A. M., Corbelli E., 2009, ApJ, 695, 937
Brown T. M., 2009, in Jogee S., Hao L., Blanc G., Marinova I., eds, ASP Conf. Ser. Vol. 419, Galaxy Evolution: Emerging Insights and Future Challenges. Astron. Soc. Pac., San Francisco, p. 110
Brown T. M., Ferguson H. C., Stanford S. A., Deharveng J.-M., 1998, ApJ, 504, 113
Bruzual G., Charlot S., 2003, MNRAS, 344, 1000
Cappellari M. et al., 2011, MNRAS, 413, 813
Ciardullo R., Rubin V. C., Ford W. K., Jr, Jacoby G. H., Ford H. C., 1988, AJ, 95, 438
Coleman G. D., Wu C.-C., Weedman D. W., 1980, ApJS, 43, 393
Courteau S., Widrow L. M., McDonald M., Guhathakurta P., Gilbert K. M., Zhu Y., Beaton R. L., Majewski S. R., 2011, ApJ, 739, 20
Crocker A. F., Bureau M., Young L. M., Combes F., 2011, MNRAS, 410, 1197
da Cunha E., Charlot S., Elbaz D., 2008, MNRAS, 388, 1595
Dalcanton J. J. et al., 2012, ApJS, 200, 18
Davidge T. J., Olsen K. A. G., Blum R., Stephens A. W., Rigaut F., 2005, AJ, 129, 201
Devereux N. A., Price R., Wells L. A., Duric N., 1994, AJ, 108, 1667
Donas J. et al., 2007, ApJS, 173, 597
Draine B. T., 2003, ARA&A, 41, 241
Draine B. T., 2011, Physics of the Interstellar and Intergalactic Medium. Princeton Univ. Press, Princeton
Draine B. T., Lee H. M., 1984, ApJ, 285, 89
Draine B. T., Li A., 2007, ApJ, 657, 810
Engelbracht C. W. et al., 2010, A&A, 518, L56
Evans I. N. et al., 2010, ApJS, 189, 37
Geehan J. J., Fardal M. A., Babul A., Guhathakurta P., 2006, MNRAS, 366, 996
Gil de Paz A. et al., 2007, ApJS, 173, 185
Gordon K. D. et al., 2006, ApJ, 638, L87
Haas M., Lemke D., Stickel M., Hippelein H., Kunkel M., Herbstmeier U., Mattila K., 1998, A&A, 338, L33
Habing H. J. et al., 1984, ApJ, 278, L59
Hernquist L., 1990, ApJ, 356, 359
Hildebrand R. H., 1983, QJRAS, 24, 267
Jacoby G. H., Ford H., Ciardullo R., 1985, ApJ, 290, 136
Kennicutt R. C., Jr, 1998, ARA&A, 36, 189

Kennicutt R. C. et al., 2011, PASP, 123, 1347
Law K.-H., Gordon K. D., Misselt K. A., 2011, ApJ, 738, 124
Leroy A. K. et al., 2011, ApJ, 737, 12
Li Z., Wang Q. D., 2007, ApJ, 668, L39
Li Z., Wang Q. D., Wakker B. P., 2009, MNRAS, 397, 148
Li Z., Garcia M. R., Forman W. R., Jones C., Kraft R. P., Lal D. V., Murray S. S., Wang Q. D., 2011, ApJ, 728, L10
Mathis J. S., Mezger P. G., Panagia N., 1983, A&A, 128, 212
Melchior A.-L., Combes F., 2011, A&A, 536, A52
Melchior A.-L., Viallefond F., Guélin M., Neininger N., 2000, MNRAS, 312, L29
Montalto M., Seitz S., Riffeser A., Hopp U., Lee C.-H., Schönrich R., 2009, A&A, 507, 283
Morganti R. et al., 2006, MNRAS, 371, 157
Mutch S. J., Croton D. J., Poole G. B., 2011, ApJ, 736, 84
Natale G. et al., 2010, ApJ, 725, 955
Nieten C., Neininger N., Guélin M., Ungerechts H., Lucas R., Berkhuijsen E. M., Beck R., Wielebinski R., 2006, A&A, 453, 459
Oke J. B., Sandage A., 1968, ApJ, 154, 21
Olsen K. A. G., Blum R. D., Stephens A. W., Davidge T. J., Massey P., Strom S. E., Rigaut F., 2006, AJ, 132, 271
Rich R. M., Corsi C. E., Cacciari C., Federici L., Fusi Pecci F., Djorgovski S. G., Freedman W. L., 2005, AJ, 129, 2670
Rosenfield P. et al., 2012, ApJ, 755, 131
Roussel H., 2012, preprint (arXiv:1205.2576)
Rowlands K. et al., 2012, MNRAS, 419, 2545
Saglia R. P. et al., 2010, A&A, 509, A61
Saintonge A. et al., 2011, MNRAS, 415, 32
Shetty R., Kauffmann J., Schnee S., Goodman A. A., 2009a, ApJ, 696, 676
Shetty R., Kauffmann J., Schnee S., Goodman A. A., Ercolano B., 2009b, ApJ, 696, 2234
Smith M. W. L. et al., 2012, ApJ, 748, 123
Soifer B. T., Rice W. L., Mould J. R., Gillett F. C., Rowan-Robinson M., Habing H. J., 1986, ApJ, 304, 651
Stanek K. Z., Garnavich P. M., 1998, ApJ, 503, L131
Tabatabaei F. S., Berkhuijsen E. M., 2010, A&A, 517, A77
Thilker D. A. et al., 2005, ApJ, 619, L67
Voit G. M., 1991, ApJ, 379, 122
Walterbos R. A. M., Kennicutt R. C., Jr, 1987, A&AS, 69, 311
Weingartner J. C., Draine B. T., 2001, ApJ, 548, 296
Young L. M. et al., 2011, MNRAS, 414, 940

APPENDIX A: THE BULGE RADIATION FIELD

For the bulge radiation field we first need the stellar luminosity distribution (which we label $\nu_\star(r)$). For this we follow Geehan et al. (2006) and use a Hernquist (1990) mass profile due to its simple spherical geometry and assume a constant mass-to-light ratio, giving

$$\nu_\star(r) = \frac{L_\mathrm{b}}{2\pi r_\mathrm{b}^3} \frac{1}{(r/r_\mathrm{b})(1+r/r_\mathrm{b})^3}. \tag{A1}$$

Geehan et al. (2006) found the bulge radius to be 0.61 kpc (their equation 1 and table 2), and we used the determined unattenuated stellar luminosity within 1 kpc of $L_\star = \sim 10^{9.9}\,\mathrm{L}_\odot$ (from Section 3.3) to normalize L_b to $10^{10.32}\,\mathrm{L}_\odot$.

The ISRF in the bulge ($\mathrm{ISRF_b}$) is then simply the luminosity density (in e.g. $\mathrm{L}_\odot\,\mathrm{pc}^3$) convolved with spherical dilution, $1/r^2$:

$$\begin{aligned} U_*(r) &= \nu_\star(r) \frac{1}{4\pi r^2 c} \\ &= \int_V \nu_\star(r_0) \frac{1}{4\pi(\boldsymbol{r}_0 - \boldsymbol{r})^2 c}\,\mathrm{d}V, \end{aligned} \tag{A2}$$

where the factor $1/c$ is introduced to convert the $\mathrm{ISRF_b}$ to an energy density (i.e. $\mathrm{erg\,cm}^{-3}$). As both the luminosity density and dilution are purely radial functions, the volume integral in equation (A2) reduces to (in spherical coordinates)

$$\begin{aligned} U_*(r) &= \int_0^\infty \frac{\nu_\star(r_0)}{4\pi c} \int_0^{2\pi} \int_0^{\pi} \frac{r_0^2 \sin\phi}{r_0^2 - 2 r r_0 \cos\phi + r^2} \mathrm{d}\phi\,\mathrm{d}\theta\,\mathrm{d}r_0 \\ &= \int_0^\infty \nu_\star(r_0) \frac{r_0}{2rc} \ln\left(\frac{r+r_0}{|r-r_0|}\right) \mathrm{d}r_0. \end{aligned} \tag{A3}$$

Substitution of equation (A1) into this and condensing then gives

$$U_*(r) = \frac{L_\mathrm{b}}{4\pi r_\mathrm{b} c} \frac{1}{r} \int_0^\infty \frac{\ln\left(\frac{r/r_\mathrm{b}+x}{|r/r_\mathrm{b}-x|}\right)}{(1+x)^3}\,\mathrm{d}x, \tag{A4}$$

where x has been substituted for r_0/r_b. The factor in front of $1/r$ and the integral equals $3.66 \times 10^{-11}\,\mathrm{erg\,cm}^{-3}$ for our given L_b and r_b, with r in kiloparsec. While the integral in equation (A4) can be analytically determined, we use a numerical integration for simplicity within this work.

This paper has been typeset from a TEX/LATEX file prepared by the author.